# Journal Pre-proof

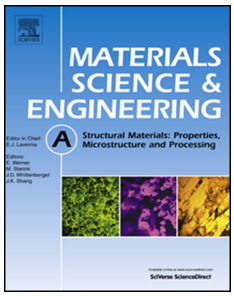


Effect of hydrogen on the embrittlement susceptibility of Fe-22Mn-0.6C TWIP steel revealed by *in-situ* tensile tests

Dong Wang, Xu Lu, Di Wan, Xiaofei Guo, Roy Johnsen

PII: S0921-5093(20)31701-9

DOI: https://doi.org/10.1016/j.msea.2020.140638

Reference: MSA 140638

To appear in: *Materials Science & Engineering A*

Received Date: 21 September 2020

Revised Date: 3 December 2020

Accepted Date: 3 December 2020

Please cite this article as: D. Wang, X. Lu, D. Wan, X. Guo, R. Johnsen, Effect of hydrogen on the embrittlement susceptibility of Fe-22Mn-0.6C TWIP steel revealed by *in-situ* tensile tests, *Materials Science & Engineering A*, https://doi.org/10.1016/j.msea.2020.140638.

## CRediT author statement

## For "Effect of hydrogen on the embrittlement susceptibility of Fe-22Mn-0.6C TWIP steel revealed by *in-situ* tensile tests"

Dong Wang[a]*, Xu Lu[a], Di Wan[a], Xiaofei Guo[b]**, Roy Johnsen[a]

**Dong Wang**: Conceptualization, Methodology, Formal analysis, Data Curation, Writing - Original Draft

**Xu Lu**: Formal analysis, Data Curation, Writing - Review & Editing

**Di Wan**: Formal analysis, Writing - Review & Editing

**Xiaofei Guo**: Formal analysis, Conceptualization, Resources, Writing - Review & Editing

**Roy Johnsen**: Formal analysis, Writing - Review & Editing

# Effect of hydrogen on the embrittlement susceptibility of Fe-22Mn-0.6C TWIP steel revealed by *in-situ* tensile tests

Dong Wang[a]*, Xu Lu[a], Di Wan[a], Xiaofei Guo[b]**, Roy Johnsen[a]

[a] Department of Mechanical and Industrial Engineering, Norwegian University of Science and Technology, Richard Birkelands vei 2B, N-7491 Trondheim, Norway

[b] Steel Institute, RWTH Aachen University, Intzestraße 1, 52072 Aachen, Germany

*Corresponding author. E-mail : dong.wang@ntnu.no

**Corresponding author. E-mail : xiaofei.guo@iehk.rwth-aachen.de



## Abstract

The hydrogen embrittlement (HE) behavior on a Fe-22Mn-0.6C twinning-induced plasticity (TWIP) steel was investigated by tensile tests with *in-situ* scanning electron microscope observation combined with electron backscatter diffraction (EBSD) and electron channeling contrast imaging (ECCI) techniques. The tensile test specimens were cathodically pre-charged with hydrogen for 0, 50, 150, and 300 hours, which accumulatively reduced the mechanical properties and induced a ductile-to-brittle fracture transition. The threshold of hydrogen content to trigger this ductile-to-brittle transition was further determined by combined thermal desorption spectroscopy (TDS) analysis and theoretical hydrogen diffusion calculation. During the tensile tests, intergranular secondary cracks were observed on the gauge surfaces of the specimens with pre-charged hydrogen. The low angle grain boundaries (LAGBs) exhibited better resistance to both crack initiation and propagation compared with high angle grain boundaries (HAGBs). In addition, the stress concentration together with the hydrogen effect on grain boundaries intersected with deformation twins are proposed as the reasons for the crack initiation and propagation.

**Keywords:** Twinning-induced plasticity (TWIP) steel; Hydrogen embrittlement (HE); Deformation twinning; Secondary cracks; Electron backscatter diffraction (EBSD); Electron channeling contrast imaging (ECCI)

## 1. Introduction

High manganese twinning induced plasticity (TWIP) steels are drawing increasing attention in automobile and construction industries due to their excellent combination of high strength and good ductility [1-3]. The outstanding mechanical properties of TWIP steels have been revealed as a result of mechanical twin formation and dynamic strain aging effect during plastic deformation due to its relatively low stacking fault energy (SFE, between 20 and 40 $mJ/m^2$ at room temperature) [4]. With this low SFE, the mobility of dislocations is reduced and the work hardening capacity is enhanced. However, the catastrophic degradation of mechanical properties has been reported on TWIP steels at hydrogen-containing environment known as hydrogen embrittlement (HE) phenomenon [5-7]. The HE is a crucial problem that needs to be urgently solved on TWIP steels before further practical use.

Up to now, the HE on different types of high-Mn steels has been studied by a large variety of experimental methods such as tensile test [8, 9], deep drawing cup test [10], nanoindentation test [11] and microcantilever bending test [12]. These tests were performed at different scales focusing on the effect of grain size, alloying elements, dissolved hydrogen concentration, and strain rate on the HE behaviors. Specifically, the HE resistance decreases with grain refinement [8, 13], addition of Al and Cu [10, 14], decreasing diffusible hydrogen content [12], and increasing strain rate [15, 16]. With further fractographic analysis, critical *in-situ* observations, and computational simulations, several mechanisms have been proposed, among which the hydrogen-enhanced localized plasticity (HELP) [17, 18], hydrogen-enhanced decohesion (HEDE) [19, 20], adsorption-induced dislocation emission (AIDE) [21, 22], and hydrogen-enhanced strain-induced vacancy formation (HESIV) [23, 24] are the most popular ones.

The HELP mechanism was first introduced by Beachem [17, 25], who analyzed the interaction between hydrogen and dislocations through *in-situ* transmission electron microscopy (TEM) observations. The main idea is that hydrogen atoms surrounding the dislocations can effectively shield the stress field of dislocations in certain directions and lead to slip planarity in those soft directions. Moreover, hydrogen atoms accumulated around the crack tip facilitate dislocation activities and lead to the formation of localized plastic zones, enhancing the crack propagation. The HEDE mechanism proposes that the cohesive energy decreases when hydrogen is trapped at the grain boundaries, second phase interfaces, and cleavage planes [26]. Consequently, these areas become the most vulnerable sites that undergo cracking under stress. The AIDE mechanism states that the hydrogen adsorbed at the crack tip weakens interatomic bonds and thereby facilitates dislocation nucleation and microvoid formation ahead of the crack tip and further contributes to crack growth [21]. The HESIV model proposed by Nagumo [24] shifted the viewpoint of the research community from hydrogen to hydrogen-enhanced strain-induced formation of vacancies. This mechanism has been proven in many cases of face-centered cubic (FCC) austenitic steels

[27-29]. Specifically, it suggests that hydrogen enhances the density and clustering of vacancies, which coalesce to microvoids and further combine as larger voids, thereby decreasing the ductile crack growth resistance. Despite extensive studies and debates, consensus could not be reached on the HE behavior, since it is a complex process depending heavily on the applied environment and material structure. Moreover, the aforementioned mechanisms are not completely distinct but share overlaps with each other [22].

In this study, the effect of hydrogen on a Fe-22Mn-0.6C TWIP steel was evaluated by tensile test with different amounts of pre-charged hydrogen under *in-situ* scanning electron microscope (SEM) observation, plus further post-mortem characterizations at the microstructural level. The objective of this paper is to reveal a quantitative relationship between the fracture mode transition and the dissolved hydrogen content, to analyze the vulnerability of different types of grain boundaries to hydrogen-assisted cracking (HAC), and also to determine the mechanism of secondary crack initiation and propagation.

## 2. Experimental

The studied material is a Fe-22Mn-0.6C (wt. %) TWIP steel and its chemical composition is shown in Table 1. The material was prepared by ingot casting, followed by hot rolling and cold rolling to a thickness of 1.5 mm. It was then heat treated at 1150 °C for 5 h in an argon atmosphere to obtain large grain size for nanomechanical tests [11]. The specimens used for slow strain rate tensile (SSRT) test were cut by electrical discharge machining into a two-step dog-bone shape with gauge geometry of 5 mm × 2 mm × 1 mm as shown in Figure 1. Prior to the hydrogen charging, the sample surface was ground sequentially from 120 to 4000 grit SiC papers and then polished with 3 μm and 1 μm diamond pastes. The surface preparation was finalized by additional polishing with colloidal silica suspension for 20 min to remove the deformation layer from the previous mechanical polishing.

The hydrogen pre-charging process was performed by using a standard electrochemical cell, which consists of a Pt net as counter electrode and an Ag/AgCl reference electrode (Ag/AgCl in saturated KCl). Hereafter, all the reported potentials in this study are versus Ag/AgCl reference electrode. The hydrogen charging was performed at 80 °C with a constant cathodic potential of -1400 mV (~10 mA/cm$^2$) in a glycerol-based electrolyte, which consists of 600 g borax (sodium tetraborate decahydrate) dissolved into 1 L glycerol. In addition, 20 vol% distilled water with 0.002 M $Na_2S_2O_3$ was added to enhance the conductivity and promote the hydrogen absorption [12]. This electrolyte has been proven to be able to preserve the sample surface from corrosion after long-time electrochemical charging [11], easing the *in-situ* observation during tensile tests without additional surface preparation. In the current study, three

different charging times of 50, 150, 300 h were applied to study the effect of different hydrogen contents on the mechanical properties.

The hydrogen content after different charging time was measured by thermal desorption spectroscopy (TDS). The TDS tests were performed using a Bruker G4 PHOENIX DH hydrogen analyzer together with a mass spectrometry detector set up (ESD 100, InProcess Instruments, Germany) at a constant heating rate of 25 °C/min from room temperature (25 °C) to 750 °C. In order to eliminate the outgassing of hydrogen, the TDS tests were started immediately after each hydrogen charging process with a dwell time of less than 5 min.

The SSRT tests were carried out by a Kammrath & Weiss tensile/compression module, which was installed into the chamber of a high-resolution field emission gun (FEG) scanning electron microscope (Quanta 650, Thermo Fisher Scientific Inc., US) for the sake of *in-situ* observation. The engineering strain rate was chosen as $4 \times 10^{-5}$ $s^{-1}$. In the current study, the proposed nominal strain value was calculated by dividing the elongation by the initial gauge length. Similarly, the dwell time between the finish of hydrogen charging and the start of tensile test was also controlled to less than 5 min to minimize the hydrogen loss. The SSRT tests were performed on two groups of charged samples: One group was loaded till fracture to study the hydrogen effect on mechanical properties and fracture mode. The other group was loaded till 10% elongation to analyze the initiation of secondary cracks on the gauge surface. The details of the testing conditions in the current study are summarized in Table 2.

Prior to the tensile tests, the microstructure of the studied material was characterized by SEM with a backscatter electron (BSE) detector as well as the electron backscatter diffraction (EBSD) technique. After the tensile tests, the same microstructural characterization process was also conducted to observe the fracture surface and gauge surface. Specifically, the fracture mode transition was determined by a detailed fractographic analysis. The EBSD measurements were conducted on the re-polished gauge surface to analyze the crystallographic information. In addition, the secondary cracks on the gauge surface in association with deformation twins were observed by the electron channeling contrast imaging (ECCI) technique, which has been proven to be an excellent tool for identifying twins, stacking faults, and dislocations based on the controlled diffraction condition with optimum contrast [6, 30]. In the current study, the ECCI was performed in the same SEM equipped with a solid-state four-quadrant BSE detector at an acceleration voltage of 30 kV with a working distance of ~6 mm. The ideal channeling contrast was obtained by tilting the specimen to an angle when the grain matrix is exactly in the Bragg condition, thus enabling the diffraction vector in a two-beam condition.

Table 1 Chemical composition of the studied Fe-22Mn-0.6C TWIP steel.

| Element | Mn | C | Nb | Ti | V | N | Al | Fe |
|---|---|---|---|---|---|---|---|---|
| wt. % | 22.60 | 0.63 | 0.03 | 0.03 | 0.108 | 0.016 | 0.008 | Bal. |

Table 2 Testing conditions in the current study.

| Testing group | Charging time/ h | Testing | Aim |
|---|---|---|---|
| 1 | 0, 50, 150, 300 | Tensile test till fracture | Mechanical properties and fractography |
| 2 | 0, 50, 150, 300 | TDS | Content of dissolved hydrogen |
| 3 | 0, 300 | Subsurface characterization | Hydrogen charging induced subsurface crack |
| 4 | 0, 50, 150, 300 | Tensile test till 10% elongation | Secondary crack initiation |

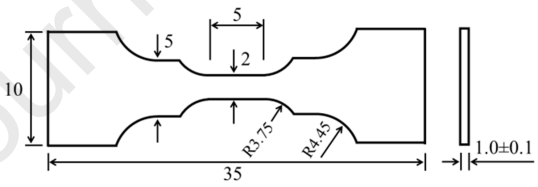


Figure 1 Geometry of the tensile sample (in mm).

## 3. Results

### 3.1 Effect of electrochemical charging on surface and subsurface

The BSE image and the normal direction-inverse pole figure (ND-IPF) map of a studied sample after surface preparation (but before hydrogen charging) are presented in Figure 2. It shows a smooth surface without any detectable scratches or cracks. The EBSD result shows a pure FCC phase with equiaxed grains containing annealing twins in the initial microstructure. The average grain size is 85 μm.

Lu et al. [31] studied the effect of electrochemical hydrogen charging on the sample surface of Ni-based alloy 718. After long-time (60-80 h) charging with a similar charging condition as the current study, the slip lines and transgranular cracks were observed on the gauge surface of alloy 718. The cracks on subsurface were also detected through cross-section analysis. Moreover, the amount and size of cracks increased as a result of longer charging time. The morphology changes due to the electrochemical charging can be a strong influencing factor in the tensile performance of the charged material. Thus, a surface check after charging is needed to avoid such influence in this study. To detect the influence of electrochemical hydrogen charging process on the sample surface and subsurface, a maximum charging time of 300 h was performed followed by subsequent gauge surface and cross-section microstructure analysis. Figure 3a and b show the SEM image and the magnified BSE image of the gauge surface after 300 h hydrogen charging. In contrast to the aforementioned observations in alloy 718, neither slip lines nor surface cracks were detected on the gauge surface of the studied TWIP sample after long time hydrogen charging. The charged specimen was further electroplated with Ni and cut from the center to obtain the cross-section surface. The cross-sectional was carefully ground and polished with different removal thickness to guarantee the reproducibility of observation. The representative BSE images of the cross-section of the sample charged for 300 h are shown in Figure 3c and d, and a defect-free subsurface without any observable cracks can be observed. Therefore, the charging process in the current study using glycerol-based electrolyte can not only protect sample surface from corrosion, easing the following *in-situ* SEM observation, but also maintain the sample integrity during hydrogen charging without forming cracks on surface and subsurface.

It needs to be mentioned here that the authors have also applied the same electrochemical charging method on two types of high-entropy alloys with pure austenitic structure, in which slip lines were generated [32] or martensitic phase transformation was detected [33] during the charging process. However, due to the different alloying systems and a relatively higher SFE (20-40 $mJ/m^2$), the currently studied TWIP steel did not show such behaviors during electrochemical charging, which can be confirmed from the SEM characterizations (Figure 3). Therefore, the performance measured in the current study is the intrinsic hydrogen influenced property of the studied material without hydrogen charging induced defects.

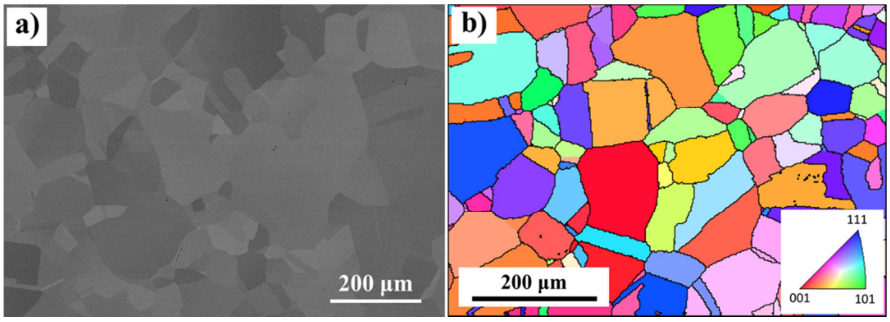


Figure 2 a) BSE image and b) ND-IPF map showing the microstructure of the studied sample.

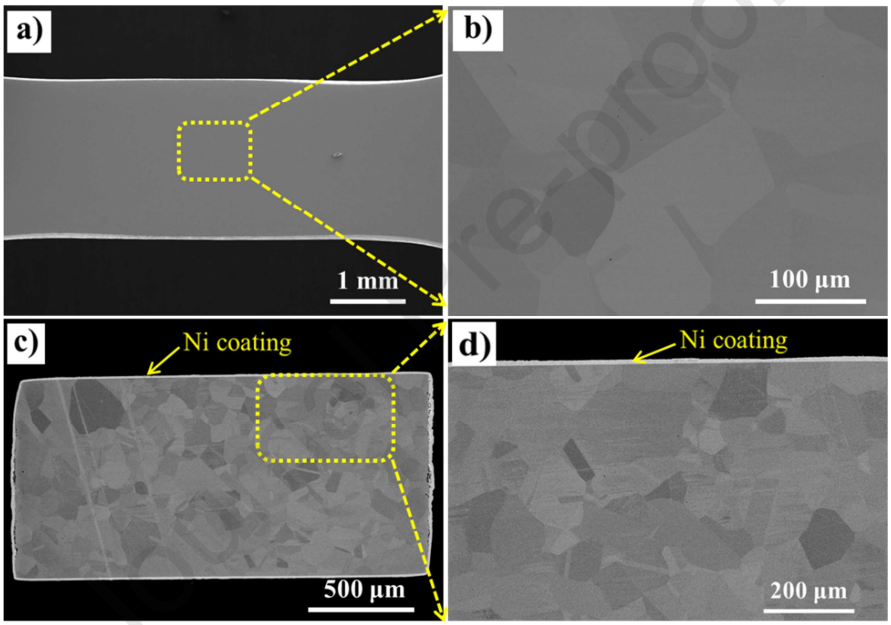


Figure 3 a) SE image of gauge surface after 300 h electrochemical hydrogen charging. b) BSE image of magnified area of (a). c) BSE image of cross-section after 300 h electrochemical hydrogen charging. d) BSE image of magnified area of c).

Another issue that needs to be taken into consideration is the segregation of sulfur (S) by the electrochemical hydrogen charging, since a S-containing poison ($Na_2S_2O_3$) has been used in the electrochemical reaction and the local segregation of S can be detrimental to the toughness of the studied material. To eliminate the possible influence of S segregation, an energy-dispersive X-ray spectroscopy (EDS) mapping was conducted on a random region of about 200 µm × 200 µm (to include several grain boundaries) on the samples before and after hydrogen charging. The SEM was operated at 10 kV with a working distance of 10 mm and an aperture of 100 µm. The spectra are shown in Figure 4. The mapping procedure took more than one hour for both cases and the spectra were the accumulated signal counts of roughly 30 k for each case. From the quantitative analyses, no substantial different can be realized

regarding the S signal of the two cases (concentration of S detected as 0 in both cases). Therefore, the current charging approach did not introduce significant change in the S concentration and thus the dominating factor in the embrittling effect should be hydrogen but not sulfur.

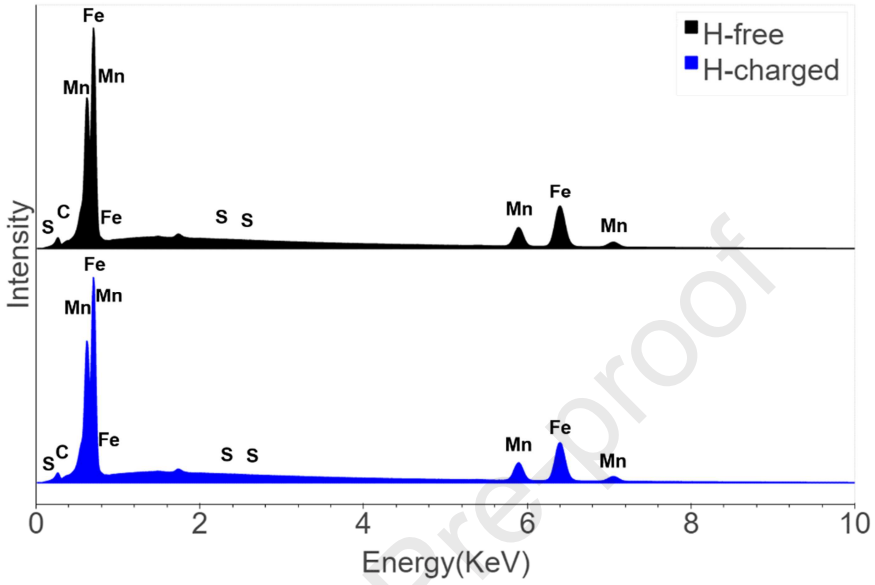


Figure 4 EDS spectra of the H-free and H-charged specimens with major elements annotated. No substantial difference can be found in the S signal between the two specimens.

3.2 Tensile tests and associated hydrogen content measurement

The tensile tests were performed inside the SEM chamber with *in-situ* SEM observation for both hydrogen-free and hydrogen pre-charged specimens. Four videos recording the testing process are presented in the supplementary documents. For the hydrogen-free specimen (as shown in Video1), a uniform elongation before the necking and fracture is presented. For the specimens charged with 50, 150, and 300 h hydrogen (as shown in Video 2, 3, and 4, respectively), secondary cracks can be clearly detected on the gauge surface after the yielding and the fracture elongations were also reduced with increased charging time. The engineering stress-strain curves of hydrogen uncharged and charged specimens are shown in Figure 5. Clear serrations can be observed on the stress-strain curves due to the dynamic strain aging effect [34], which has been proposed as a common phenomenon in TWIP steels [1, 35]. The curves show an overlapped elastic region with a same yielding strength regardless of the charged hydrogen. However, a reduction in both the tensile strength and the elongation to fracture was observed in the hydrogenated specimens, and the reduction was more significant with increased charging time. For the uncharged specimen, the fracture elongation was 77.2% and the ultimate tensile strength was 828.1 MPa. When charged with hydrogen by 50, 150, and 300 h, the fracture elongation was reduced to 62.8%, 49.1%,

and 29.6%, and the ultimate tensile strength was reduced to 747.1, 622.7, and 477.4 MPa, respectively. In addition, the corresponding mechanical degradation due to dissolved hydrogen can be described by the embrittlement factor (EF) [36] as follows:

$$\mathrm{EF} = \left(1 - \frac{\varepsilon_H}{\varepsilon_{no\ H}}\right) \times 100\% \quad (1)$$

Where $\varepsilon_H$ and $\varepsilon_{no\ H}$ indicate the engineering fracture strain of hydrogen pre-charged sample and uncharged sample, respectively. Zero is defined as the EF value at the uncharged condition and it continuously increased to 11.7%, 36.4%, and 61.7% after 50, 150, and 300 h hydrogen charging, respectively. A detailed summary of hydrogen induced mechanical property degradation is shown in Table 3.

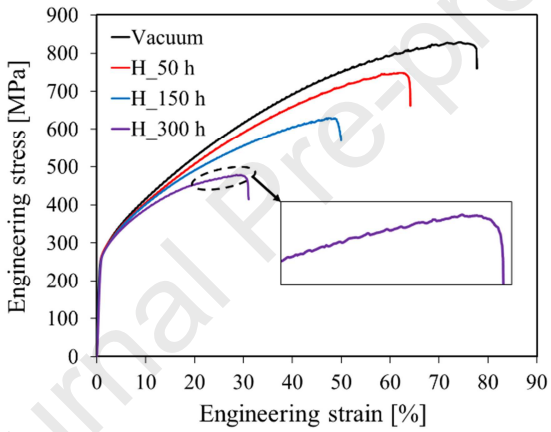


Figure 5 Engineering stress-strain curves of specimens with different hydrogen pre-charging time.

Figure 6 shows the curves of hydrogen desorption rate on the charged and uncharged samples obtained from the TDS measurements. The amount of hydrogen under the first peak at 300 °C represents diffusible hydrogen, while that under the second peak at 550-600 °C corresponds to trapped hydrogen. The original hydrogen content of uncharged sample was 0.02 wppm and the dissolved hydrogen contents were 9.39, 16.57, and 22.31 wppm after 50, 150, and 300 h of electrochemical hydrogen charging, respectively. The aforementioned hydrogen contents are the total amount of detected hydrogen from the TDS measurement, which include the hydrogen dissolved in interstitial sites and trapped in both reversible and irreversible trapping sites. With increasing charging time, the hydrogen content increases significantly, which further degrades the mechanical properties to a higher level. It is noticed that the desorption rates in Figure 6 are not zero at the end of the test for hydrogen charged samples. This is due to the fact that part of deeply trapped hydrogen cannot be extracted at 750 °C, and a higher temperature of 800-850 °C is needed to

fully extract the deeply trapped hydrogen [13]. Therefore, the reported hydrogen content leads to an underestimation of the total hydrogen contents, which was calculated as 2-3% by assuming a linear reduction on the TDS curves from the current value at 750 °C to zero at 850 °C.

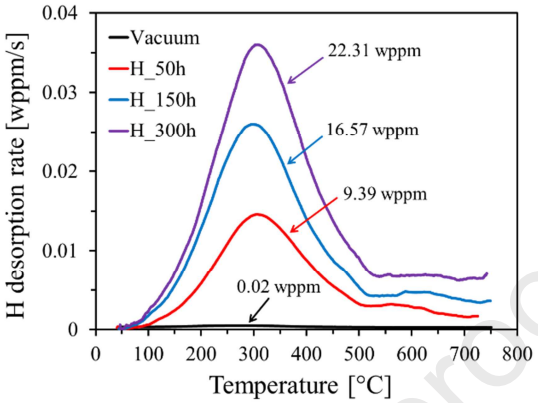


Figure 6 Hydrogen desorption rate curves of hydrogen uncharged and charged samples.

Table 3 Properties of the studied materials under different hydrogen charging conditions.

| Charging time (h) | Fracture elongation (%) | Ultimate tensile strength (MPa) | EF (%) | Brittle depth (μm) | Total measured hydrogen content (wppm) |
|---|---|---|---|---|---|
| 0 | 77.2 | 828.1 | 0 | 0 | 0.02 |
| 50 | 62.8 | 747.1 | 11.7 | 57.6 | 9.39 |
| 150 | 49.1 | 622.7 | 36.4 | 102.2 | 16.57 |
| 300 | 29.6 | 477.4 | 61.7 | 148.5 | 22.31 |

3.3 Fracture surface and gauge surface characterization

The fracture surfaces after failure are summarized in Figure 7. Figure 7a1 shows the fracture surface of the uncharged specimen and Figure 7a2 is the magnified image of the highlighted area in Figure 7a1. A notable ductile fracture surface can be observed on the uncharged sample from gauge surface to the center region with fully covered dimple structure. The fracture surface after hydrogen charging of 50, 150, and 300 h are exhibited in Figure 7b1, c1, and d1, as well as in the magnified images of Figure 7b2, c2, and d2, respectively. In contrast, brittle intergranular fracture surfaces were observed at the areas near sample surface. Clearly, the ductile fracture mode was transformed to intergranular fracture mode after hydrogen charging with an observable transition boundary marked as blue dashed lines in Figure 7b1, c1, and d1. In addition, the intergranular fracture was more pronounced with a longer charging time. The depths of the

intergranular zone were measured as 57.6, 102.2, and 148.5 μm after 50, 150, and 300 h hydrogen charging, respectively.

As exhibited in the *in-situ* tensile test videos in the supplementary documents, the fracture happened with a crack initiated from one side of specimen edge and propagated to the other side as the main or primary crack. The direction of the main crack propagation was nearly perpendicular to the tensile direction. In addition, a considerable number of secondary cracks were formed parallel to the main crack on the hydrogen charged samples (Figure 8b) after the yielding point. Figure 8a summarizes the crack surface density at different charging conditions throughout the whole tensile tests. The crack surface density is defined as the ratio between the sum of the crack lengths and the total area. For each step, the crack surface density was analyzed on three regions of 1.5×1.5 $mm^2$ using ImageJ software to minimize the statistical discrepancy. The result shows that there was no detectable secondary crack on the uncharged sample (Figure 8c), while the crack surface density on the charged samples increased with larger strain. Moreover, the crack surface density on the sample with longer charging time was larger than that with shorter charging time, and this difference became more pronounced along the tensile elongation.

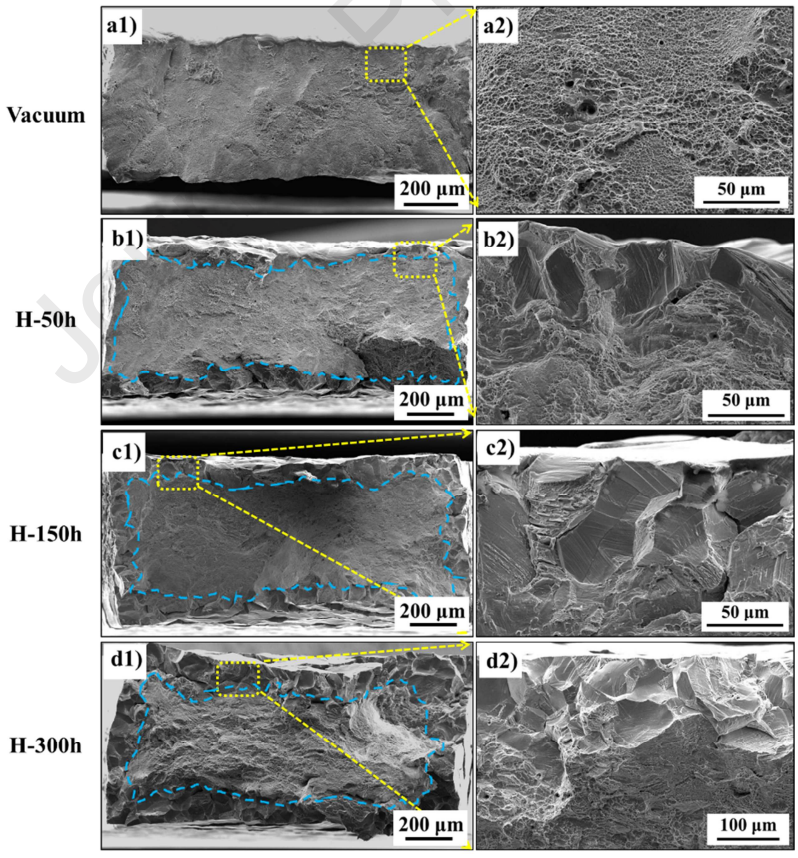


Figure 7 Fracture surface of the tensile tested samples with and without hydrogen pre-charging. a) Fracture surface of reference sample without hydrogen charging. Fracture surface of samples after b) 50 h, c) 150 h, and d) 300 h

hydrogen charging. a2), b2), c2) and d2) are the higher magnification details from the areas marked by the yellow rectangles in a1), b1), c1) and d1), respectively. The blue dashed lines in a1), b1), c1) and d1) describe the transition boundary between brittle and ductile fracture.

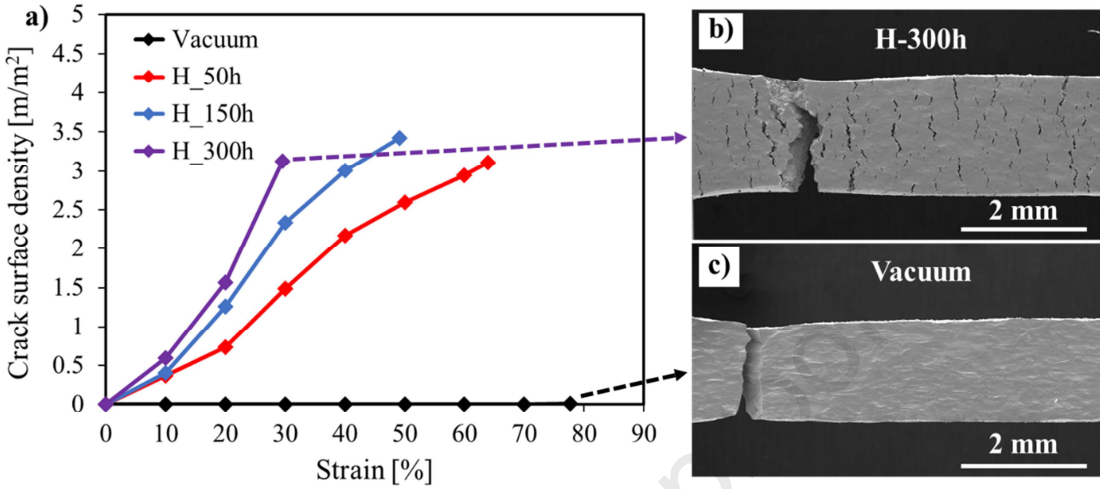


Figure 8 (a) The evolution of crack surface density at different charging conditions. The fracture gauge surface of sample with 300 h pre-charged hydrogen (b) and without hydrogen charging (c).

Figure 9 shows the SEM image with the corresponding EBSD characterizations of typical secondary cracks on gauge surface after failure on the specimen with 300 h pre-charged hydrogen. The paths of secondary surface cracks are in general perpendicular to the global tensile direction. To investigate the secondary cracks at a microstructural level, EBSD scan was performed in the area highlighted in Figure 9a. It can be seen from Figure 9b that the secondary cracks have been initiated at the grain boundaries and propagated in an intergranular manner. No transgranular-type cracks can be detected. Figure 9c shows the Kernel Average Misorientation (KAM) map of the same area. This method calculates the average misorientation from the surrounding points regarding the scanned point, and this criterion is used to evaluate the local deformation and local dislocation density of each scanned point. It can be seen from the map that a higher KAM value is always found at grain boundaries, implying that grain boundary is a favored place for deformation concentration. Along cracked boundaries, the KAM value is not significantly higher than the deformation-concentrated areas along non-cracked boundaries and the area with higher KAM value is rather confined to the cracks, suggesting a brittle cracking manner with limited plastic deformation mechanism. Figure 9d shows the boundary map over the same area with high angle grain boundaries (HAGBs, >15°), low angle grain boundaries (LAGBs, 2-15°) and twin boundaries. The LAGBs appear at the places roughly the same as the deformation-concentrated areas revealed by the KAM map, indicating a deformation-nature of the LAGBs. An interesting feature is that most of the

intergranular cracks are connected to some twin boundaries. Most of the intersecting twins are mechanical twins since they appear as thin bands. No clear dependency can be found on the annealing twins.

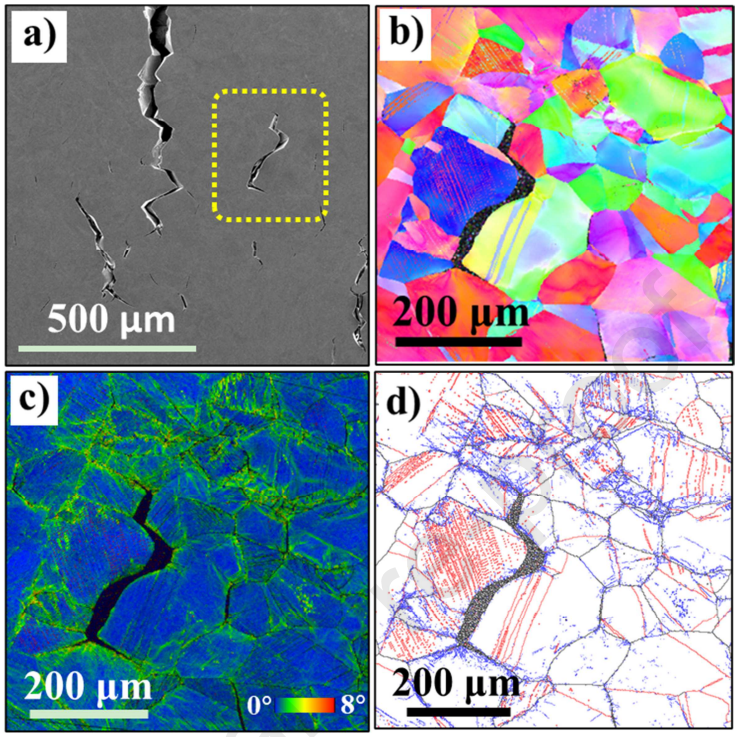


Figure 9 a) SEM image showing surface cracks; b) ND-IPF map; c) KAM map and d) boundary map with black lines showing HAGB, blue lines showing LAGB and red lines showing twin boundary. b)-d) are the same area as highlighted in a). The tensile direction is horizontal for all images.

## 4. Discussion

### 4.1 Hydrogen influence on the strength

The general hydrogen influence on the mechanical performance of metallic materials is a decrease in the ductility, referred as embrittlement effect. However, the hydrogen influence on the strength is not clear yet. Different studies have shown different effects including both hardening [37, 38] and softening [39, 40]. But a common agreement has not been reached yet.

To estimate the effect of hydrogen on the strength of the material in the current study, true stress - true strain curves are needed. The solid curves in Figure 10 are the calculated true stress - true strain curves based on the conventional approach by assuming a constant gauge volume during tension until necking happens (*i.e.* when the geometrical softening is in equilibrium with the work hardening, as can be estimated by the Considère criterion). From the solid curves, a decreasing true stress is displayed for all

three hydrogen-charged specimens, showing a “softening-like” behavior. However, since the hydrogen-induced crack formation on the gauge surface during tension is detected (as shown in the video 2-4 in the supplementary documents), which makes the estimated cross-section area larger than the real case, the assumption of “constant gauge volume” becomes invalid and the conventional method of calculating true stress becomes improper. As a result, the calculated true stress values would be underestimated. To improve the accuracy of the estimation, starting from the definition of the “stress”, correct load value and correct area of the cross-section are needed. An assumption is thus made here: the ductile area on the fracture surface indicates the area of the cross-section at the maximum load, while the brittle area on the fracture surface has been developing before reaching the maximum load. Therefore, we took **the maximum load** divided by **the ductile fracture area** as the true UTS value. By this method, the calibrated true UTS values are shown as solid diamonds in Figure 10. Worthy of note, the true UTS value of the hydrogen-free specimen from this method shows good agreement with the value from conventional method (*i.e.* the black diamond data point fits well with the maximum true stress value of the black solid curve). However, the hydrogen-charged cases show higher true UTS values than the conventional curves. The dashed curves are plotted to estimate the true stress in the intermediate stage. It needs to mention here that the method for calculating the true UTS value in the current study does not consider the effect of high triaxiality levels in the ligament induced by the secondary cracks. As a result, the obtained true UTS values are overestimated than that for a smooth tensile bar having the same minimum cross-section area [41]. Though these curves cannot correctly reflect the real true stress, they can be used to express the continuous evolution of the values in this stage. Based on these curves, surprisingly, a hardening effect of hydrogen instead of softening is clearly observed at a same strain level. With the increasing hydrogen-charging time (referring to a higher hydrogen content), the hardening effect becomes more considerable. Recently, the effect of hydrogen on strength has also been studied by fatigue crack growth testing showing a hydrogen-restricted plasticity evolution [42], nanoindentation testing showing a hydrogen-enhanced lattice friction [11] and micro-pillar compression test showing a hydrogen-increased stress level [43]. These studies as well as the current work show a similar hardening effect of hydrogen on different metallic materials.

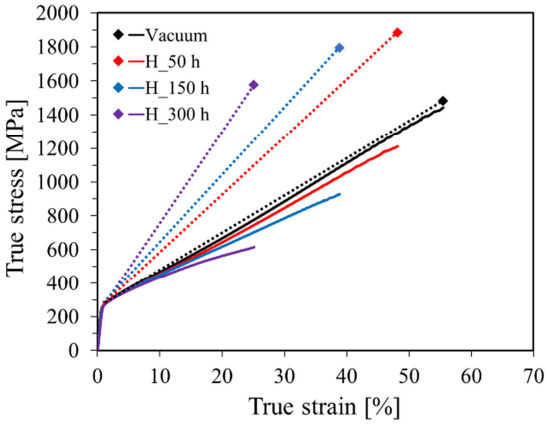


Figure 10 True stress - true strain curves of specimens with different amounts of pre-charged hydrogen. The diamond data points are the true UTS values.

It worth mentioning that the strain hardening behavior of the studied TWIP steel is an important factor for its excellent mechanical properties (when hydrogen-induced secondary cracks are absent) and has been intensely studied in literature (*e.g.* [44]). The mechanisms during plastic deformation such as mechanical twinning and dynamic strain aging can have a substantial impact on the plasticity evolution. However, due to the secondary surface cracks in some hydrogen-charged cases such as the current work, the suitable approach to evaluate the true stress has not been well established yet and thus a deep discussion on this point might be controversial and inconsequential. The authors have planned a quantitative refined study on the real area of the cross-section during the deformation of hydrogen-charged specimens by using 3D tomography technique combined with finite-element modelling in determining the more accurate stress response (and therefore reflecting the correct work hardening behavior), and this will be realized in the near future.

4.2 Hydrogen induced fracture mode transition

The hydrogen contents after different pre-charging periods were measured by TDS tests and the corresponding values are shown in Figure 6. The concentration of hydrogen on the sample surface $C_s$ can be estimated based on the total dissolved hydrogen content according to the method proposed by Pontini and Hermida [45] as follows:

$$C_s = \frac{\omega C_M}{4}\sqrt{\frac{\pi}{Dt}} \qquad (2)$$

where $\omega$ is the sample thickness, $C_M$ is the total dissolved hydrogen content measured by TDS tests, $t$ is the hydrogen pre-charging time, and $D$ is the hydrogen diffusion coefficient at the charging temperature of 80 °C. The $D$ value used in Eq. 2 was calculated as $4.36\times10^{-15}$ $m^2/s$ by setting diffusion activation

energy as 30.4 kJ/mol [46] and diffusion coefficient value at room temperature as $5.24\times10^{-16}$ $m^2/s$ [15]. The surface contents $C_s$ after 50, 150, and 300 h pre-charging were calculated as 145.6, 151.3, and 152.7 wppm, respectively. These values were similar with each other with a difference less than 5%. The hydrogen concentration $C(x,t)$ after different charging time $t$ at the depth of $x$ can be further calculated by using the Fick's law-based "semi-infinite" model [47]:

$$\frac{C(x,t)-C_0}{C_s-C_0}=1-\mathrm{erf}\left(\frac{x}{\sqrt{4Dt}}\right) \quad (3)$$

$$\mathrm{erf}(u)=\frac{2}{\sqrt{\pi}}\int_0^u \exp(-u^2)\,du \quad (4)$$

where $C_0$ is the original hydrogen content dissolved in specimen as 0.02 wppm as shown in Figure 6. Figure 11 shows the hydrogen concentration profiles after different pre-charging conditions with respect to depth. The hydrogen concentration exhibits considerable decrease immediately below the sample surface, which is a common feature in FCC alloys during electrochemical hydrogen charging due to their low hydrogen diffusivity [48]. The longer charging time yields a richer hydrogen content at the same depth, and a deeper hydrogen penetration depth can also be obtained.

The brittle area after different pre-charging periods can be measured from fractographies shown in Figure 7 and the corresponding depths are marked as black vertical dashed lines in Figure 11. By comparing the critical hydrogen content at the ductile-to-brittle transit boundary (see

Table 3), a common critical hydrogen content of 22 wppm can be found for each charging condition as the threshold value. This result means that the area below sample surface charged by hydrogen to the critical content (22 wppm) and above would cause brittle fracture upon further mechanical loading.

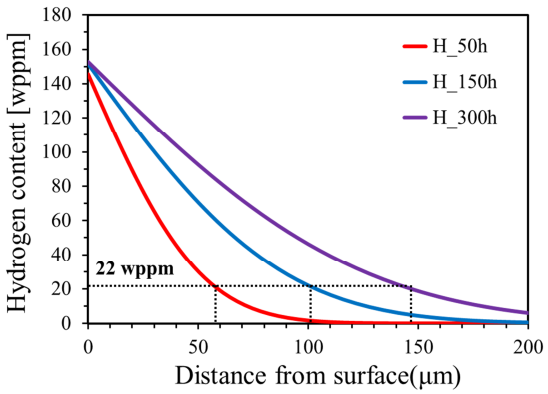


Figure 11 Hydrogen concentration profiles of samples with different pre-charging time. The black dashed lines indicate the depth of brittle fracture with corresponding hydrogen content (from

Table 3).

4.3 Hydrogen-assisted secondary crack during deformation

As illustrated in the tensile videos attached in the supplementary documents as well as the fracture surfaces shown in Figure 7, no detectable intergranular fracture was observed on the specimen without hydrogen pre-charging and the final fracture surface was pure ductile. As a contrast, the failure of the hydrogen charged specimens showed a mixture of brittle intergranular fracture near the surface and ductile transgranular dimples close to the center without any evidence of apparent necking before the failure. This behavior has been commonly observed in HE studies on other FCC alloys [9, 49]. In addition, a large number of secondary cracks were observed on the gauge surface of pre-charged samples during tensile tests. EBSD analysis (Figure 9) shows that these secondary cracks are pure intergranular. The secondary cracks along both grain boundaries and twin boundaries were reported in the former studies [6, 50, 51]. However, in the current study, all cracks were along grain boundaries and no cracks along twin boundaries were detected. This difference might come from different charging conditions and different heat treatments.

To illustrate the microstructural features on secondary crack initiation and propagation paths, the overall grain boundary distribution on the pre-charged specimens before test was statistically analyzed. Additionally, the grain boundary types of the initiated secondary cracks after 10% straining and after fracture were also analyzed to investigate the cracking preferences. Figure 12 shows the results of the aforementioned analysis on the 300 h pre-charged sample. The grain boundary distribution was characterized by EBSD mapping on the gauge surface at three stages: before tensile test, at 10% strain, and after failure. Before tensile test (Figure 12a) and after failure (Figure 12c), more than 100 original grain boundaries and secondary cracks were measured. For the stage of tensile till 10% strain, all the initiated secondary cracks on the gauge surface were characterized. Figure 12a-c show the SEM images of the three stages and Figure 12d-f illustrate the corresponding distribution of grain boundary as a function of misorientation angle.

As shown in Figure 12d, the initial microstructure contains 5.7% LAGBs and 94.3% HAGBs. Among the HAGB, a large fraction was detected between the misorientation angle of 40-45°. Figure 12e displays the fraction of cracked grain boundaries after 10% strain, a slightly larger fraction (97.4%) of cracks has been initiated at HAGBs, while only 2.6% of them has been initiated at LAGBs. In the fracture stage, 97.2% of the cracks have been propagating along HAGBs and 2.8% of them have been propagating along LAGBs, as shown in Figure 12f. Compared to the initial microstructure, it is clear that the HAGBs are more prone to crack compared to LAGBs during the tensile loading. The similar statistically values from the 10%

elongated specimen and the fractured specimen indicate that during crack propagation, the initiated cracks have not been significantly deflected to other type of GBs in a global sense. The results demonstrated the LAGBs exhibited better resistance to both crack initiation and propagation. No specific HAGB (regarding misorientation) can be determined as preferential cracking sites, since they showed a similar misorientation distribution as original microstructure. The observation of LAGB being crack initiation/propagation resistant has also been proposed in pure Ni by Bechtle et al. [52], who found that a higher proportion of LAGB reduces the hydrogen-induced intergranular embrittlement. This crack resistant property of LAGB might come from their more ordered structure, which leads to a lower local hydrogen diffusivity and thus impedes the hydrogen transportation and segregation [53]. As a result, the formation of new vacancies and the reduction of grain boundary cohesive strength are minimized. Another possible reason for the better crack resistance of LAGBs is their higher boundary separation energy [54], which makes these boundaries more resistant to fracture.

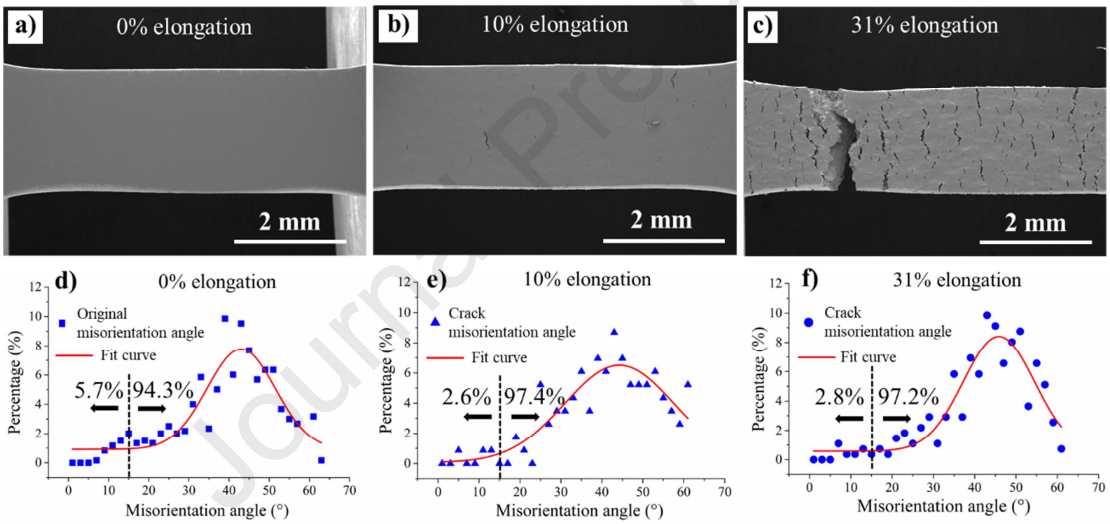


Figure 12 SEM images of specimens after 300 h hydrogen pre-charging at different strains: (a) before tensile test with 0% elongation, (b) at 10% elongation, (c) after fracture at 31% elongation. Statistical analysis of secondary crack initiation and propagation: (d) the fraction of total grain boundary types. the fraction of grain boundary types that (e) initiate cracks and (f) susceptible to crack propagation. The black dotted line in (d), (e), and (f) are the dividing line between LAGBs and HAGBs.

### 4.4 Mechanism of secondary intergranular cracking

It has been seen from the EBSD analysis that most of the typical secondary cracks are intersecting with some mechanical twins (Figure 9). However, since the step size of the EBSD scan was relatively large, some small-scale mechanical twins could not be correctly detected. To further investigate the interaction between the deformation twins and the cracked boundaries, ECCI was conducted near the cracked

boundaries. Figure 13 shows the ECC images demonstrating the initiated secondary cracks on the gauge surface of specimen with 50 h pre-charged hydrogen after 10% elongation. By tilting the specimen to an optimized contrast condition, the matrix background in ECC image appears as dark due to its low backscattering yield. While dislocations appear as white contrast on the dark background due to the interaction between dislocations and matrix surface, and the stacking faults appear as bright areas with a white straight line on one side, indicating the interaction between the stacking fault planes and the sample surface [55]. All the ECCI results show a clear intergranular crack manner as exhibited in Figure 13a1, b1, and c1. The formed cracks were along grain boundaries with impinged thick deformation twinning bands at a relative perpendicular angle (measured as 78° and 98° in Figure 13a2 and b2, respectively). The propagation of the crack with an increased opening angle can be detected at the intersections between crack and deformation twinning bands as shown in Figure 13a2. Moreover, the intergranular crack propagation was stopped when no further deformation twinning bands intersect with the grain boundary, as shown in Figure 13b2 and c2. Figure 13b2 shows a stoppage of crack when the grain boundary intersects only with stacking faults, and Figure 13c2 exhibits the grain boundary without initiated cracks when only a small quantity of thin deformation twins was intersected. This indicates that the grain boundaries intersected with thick deformation twinning bands act as the preferential sites for crack initiation and propagation paths. In addition, the intersection angle between deformation twinning band and grain boundary is also a decisive factor for the crack initiation. As shown in Figure 13c1, parallel twinning bands intersecting with a curved grain boundary at different angles. When the low intersect angle (28°) was applied, no initiated cracks can be detected even at the triple junction of grain boundaries, which was proposed to be more vulnerable to hydrogen-assisted intergranular cracking due to the stress concentration [56]. By contrast, cracks (Figure 13c1) were observed when the intersection angle increased to a value that close to perpendicular angle. Specifically, a crack was detected at the high intersect angle (76°) within the same system containing a same grain boundary and an even thinner deformation band compared with the non-crack sites shown above. Furthermore, a local stress relief could be expected from the cracking event at the grain boundary - 76° twinning band intersection, which made the cracking even more difficult at the triple junction - 28° twinning band intersection.

The stress concentration together with the hydrogen effect on grain boundaries intersecting with thick deformation twins are the reasons for the crack initiation and propagation. The deformation twin induced grain boundary failure has been demonstrated by both experimental work [57] and molecular dynamics simulation [58]. It proposed that high stress concentration, high dislocation density, and high lattice rotation would be developed at the grain boundaries intersected with deformation twins due to the incompatible plastic deformation. A recent study has shown that the stress concentration induced by mechanical twinning intercepting with GBs is high enough to initiate the plastic deformation both in the

original grain and in the neighboring grain [59]. Moreover, a thicker deformation twin results in a higher concentrated stress, leading to intergranular cracking by nucleation of microcracks and coalescence of voids. On the other hand, grain boundaries are known as preferential sites for hydrogen trapping and segregation [60]. The large amount of segregated hydrogen on the grain boundary would promote the vacancies formation [61] and reduce the grain boundary cohesive energy [62], which further results in intergranular failure.

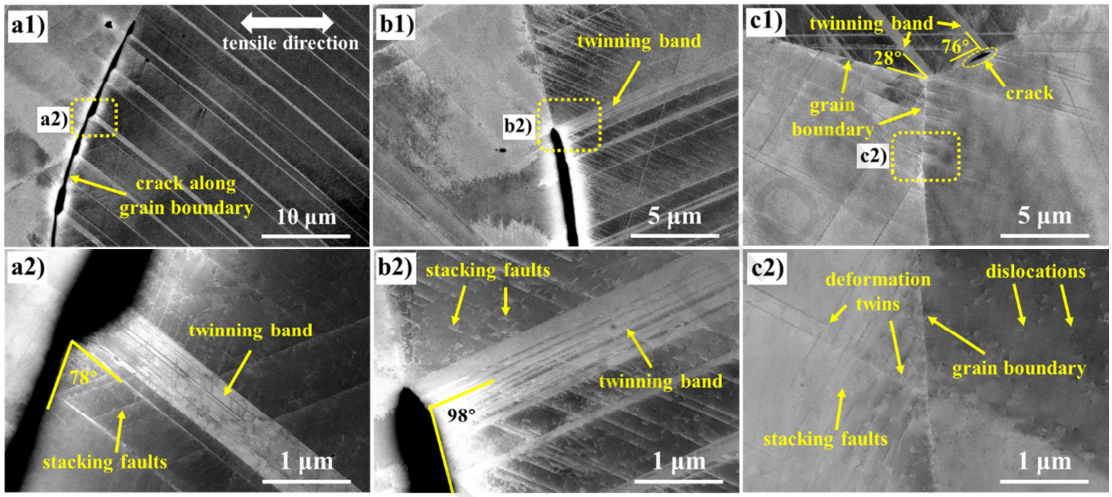


Figure 13 ECC images showing the intergranular secondary cracks on the gauge surface of specimen with 50 h pre-charged hydrogen at 10% strain. The tensile direction is along horizontal direction for all images. a2), b2), and c2) show the areas highlighted by yellow rectangles in a1), b1), and c1), respectively.

## 5. Conclusions

In this study, the susceptibility of HE on Fe-22Mn-0.6C TWIP steel was investigated by tensile tests with *in-situ* SEM observation. The tests were performed on non-charged specimen and on hydrogen pre-charged specimens with different pre-charging time (50, 150, and 300 h). By further using TDS hydrogen content measurement and post-mortem SEM, EBSD and ECCI characterizations, the following conclusions can be drawn:

1. The presence of hydrogen has detrimental effects on both the tensile strength and fracture elongation. The fracture surface of the uncharged sample was pure ductile with fully covered dimple structure. By contrast, brittle intergranular fracture surface was observed in the vicinity of sample surface on hydrogen charged samples. Moreover, a longer charging time results in a higher dissolved hydrogen content. The different amounts of charged hydrogen showed an accumulatively effect on the mechanical property

degradation and led to thicker brittle featured layer. A specific amount of hydrogen (22 wppm) was determined as the threshold value for this ductile-to-brittle transition.

2. During the tensile tests, the secondary cracks on gauge surface were detected only on the charged specimens. All these cracks were nucleated on the grain boundaries and propagated in an intergranular manner. The amount and area occupation of secondary cracks increased as the increasing of charging time and tensile elongation. By further statistical analysis on the secondary cracks, it shows that the LAGBs have a better resistance to crack initiation and propagation compared with the HAGBs.

3. The grain boundaries that intersect with thick deformation twins are the preferential crack initiation sites and propagation paths. This is due to the stress concentration at these intersecting points in combination with the intrinsic hydrogen effect on grain boundaries. The intersecting angle can influence the stress concentration and thus influence the cracking behaviors.

**Acknowledgements**

The authors are grateful for the support provided by Research Council of Norway through the HyF-Lex (244068/E30) project and the HyLINE (294739) project, and the promotion of scientific exchange by German Research Foundation in the framework of Collaborative Research Center SFB 761 “Steel - ab initio”. The authors thank Prof. Afrooz Barnoush for the discussion regarding the hydrogen hardening behavior in section 4.1. The author (Dong Wang) would like to acknowledge the financial support from the China Scholarship Council.

**Data availability**

The data that support the findings of this study are available on request from the corresponding author. The data are not publicly available as the data also forms part of an ongoing study.

**References**

[1] B.C. De Cooman, Y. Estrin, S.K. Kim, Twinning-induced plasticity (TWIP) steels, Acta Mater. 142 (2018) 283-362.
[2] O. Grassel, L. Kruger, G. Frommeyer, L.W. Meyer, High strength Fe-Mn-(Al, Si) TRIP/TWIP steels development-properties-application, Int. J. Plast. 16(10-11) (2000) 1391-1409.
[3] S. Curtze, V.T. Kuokkala, Dependence of tensile deformation behavior of TWIP steels on stacking fault energy, temperature and strain rate, Acta Mater. 58(15) (2010) 5129-5141.
[4] D.T. Pierce, J.A. Jiménez, J. Bentley, D. Raabe, J.E. Wittig, The influence of stacking fault energy on the microstructural and strain-hardening evolution of Fe–Mn–Al–Si steels during tensile deformation, Acta Mater. 100 (2015) 178-190.
[5] M. Koyama, E. Akiyama, Y.K. Lee, D. Raabe, K. Tsuzaki, Overview of hydrogen embrittlement in high-Mn steels, Int. J. Hydrog. Energy 42(17) (2017) 12706-12723.
[6] M. Koyama, E. Akiyama, K. Tsuzaki, D. Raabe, Hydrogen-assisted failure in a twinning-induced plasticity steel studied under in situ hydrogen charging by electron channeling contrast imaging, Acta Mater. 61(12) (2013) 4607-4618.
[7] Q.L. Liu, Q.J. Zhou, J. Venezuela, M.X. Zhang, J.Q. Wang, A. Atrens, A review of the influence of hydrogen on the mechanical properties of DP, TRIP, and TWIP advanced high-strength steels for auto construction, Corros. Rev. 34(3) (2016) 127-152.
[8] Y. Bai, Y. Momotani, M.C. Chen, A. Shibata, N. Tsuji, Effect of grain refinement on hydrogen embrittlement behaviors of high-Mn TWIP steel, Mater. Sci. Eng. A 651 (2016) 935-944.
[9] M. Koyama, E. Akiyama, K. Tsuzaki, Hydrogen embrittlement in a Fe-Mn-C ternary twinning-induced plasticity steel, Corros. Sci. 54 (2012) 1-4.
[10] K.G. Chin, C.Y. Kang, S.Y. Shin, S. Hong, S. Lee, H.S. Kim, K.H. Kim, N.J. Kim, Effects of Al addition on deformation and fracture mechanisms in two high manganese TWIP steels, Mater. Sci. Eng. A 528(6) (2011) 2922-2928.
[11] D. Wang, X. Lu, Y. Deng, X. Guo, A. Barnoush, Effect of hydrogen on nanomechanical properties in Fe-22Mn-0.6C TWIP steel revealed by in-situ electrochemical nanoindentation, Acta Mater. 166 (2019) 618-629.
[12] X. Lu, D. Wang, Z. Li, Y. Deng, A. Barnoush, Hydrogen susceptibility of an interstitial equimolar high-entropy alloy revealed by in-situ electrochemical microcantilever bending test, Mater. Sci. Eng. A 762 (2019) 138114.
[13] N. Zan, H. Ding, X.F. Guo, Z.Y. Tang, W. Bleck, Effects of grain size on hydrogen embrittlement in a Fe-22Mn-0.6C TWIP steel, Int. J. Hydrog. Energy 40(33) (2015) 10687-10696.
[14] Y.J. Kwon, T. Lee, J. Lee, Y.S. Chun, C.S. Lee, Role of Cu on hydrogen embrittlement behavior in Fe-Mn-C-Cu TWIP steel, Int. J. Hydrog. Energy 40(23) (2015) 7409-7419.
[15] Y.J. Kwon, H.J. Seo, J.N. Kim, C.S. Lee, Effect of grain boundary engineering on hydrogen embrittlement in Fe-Mn-C TWIP steel at various strain rates, Corros. Sci. 142 (2018) 213-221.
[16] B. Bal, M. Koyama, G. Gerstein, H.J. Maier, K. Tsuzaki, Effect of strain rate on hydrogen embrittlement susceptibility of twinning-induced plasticity steel pre-charged with high-pressure hydrogen gas, Int. J. Hydrog. Energy 41(34) (2016) 15362-15372.
[17] H.K. Birnbaum, P. Sofronis, Hydrogen-enhanced localized plasticity—a mechanism for hydrogen-related fracture, Mater. Sci. Eng. A 176(1) (1994) 191-202.
[18] P. Ferreira, I. Robertson, H. Birnbaum, Hydrogen effects on the interaction between dislocations, Acta Mater. 46(5) (1998) 1749-1757.
[19] W. Gerberich, Modeling hydrogen induced damage mechanisms in metals, in: R.P. Gangloff, B.P. Somerday (Eds.), Gaseous Hydrogen Embrittlement of Materials in Energy Technologies, Woodhead Publishing2012, pp. 209-246.
[20] Z. Tarzimoghadam, M. Rohwerder, S.V. Merzlikin, A. Bashir, L. Yedra, S. Eswara, D. Ponge, D. Raabe, Multi-scale and spatially resolved hydrogen mapping in a Ni-Nb model alloy reveals the role of the δ phase in hydrogen embrittlement of alloy 718, Acta Mater. 109 (2016) 69-81.

[21] S.P. Lynch, Environmentally Assisted Cracking: Overview of Evidence for an Adsorption-Induced Localized-Slip Process, Acta Metall. 36(10) (1988) 2639-2661.
[22] S. Lynch, Hydrogen embrittlement phenomena and mechanisms, Corros. Rev. 30(3-4) (2012) 105-123.
[23] S. Hinotani, Y. Ohmori, F. Terasaki, Effect of Nickel on Hydride Formation and Hydrogen Embrittlement in Ni-Cr-Fe Alloys, Mater. Sci. Eng. 74(2) (1985) 119-131.
[24] M. Nagumo, Hydrogen related failure of steels - a new aspect, Mater. Sci. Technol. 20(8) (2004) 940-950.
[25] I.M. Robertson, The effect of hydrogen on dislocation dynamics, Eng. Fract. Mech. 68(6) (2001) 671-692.
[26] L.B. Pfeil, The effect of occluded hydrogen on the tensile strength of iron, Proceedings of the Royal Society of London. Series A, Containing Papers of a Mathematical and Physical Character 112(760) (1926) 182-195.
[27] D.G. Xie, S.Z. Li, M. Li, Z.J. Wang, P. Gumbsch, J. Sun, E. Ma, J. Li, Z.W. Shan, Hydrogenated vacancies lock dislocations in aluminium, Nat. Commun. 7 (2016).
[28] A. Metsue, A. Oudriss, X. Feaugas, Trapping/detrapping kinetic rates of hydrogen around a vacancy in nickel and some consequences on the hydrogen-vacancy clusters thermodynamic equilibrium, Comp. Mater. Sci. 151 (2018) 144-152.
[29] M. Hatano, M. Fujinami, K. Arai, H. Fujii, M. Nagumo, Hydrogen embrittlement of austenitic stainless steels revealed by deformation microstructures and strain-induced creation of vacancies, Acta Mater. 67 (2014) 342-353.
[30] S. Zaefferer, N.N. Elhami, Theory and application of electron channelling contrast imaging under controlled diffraction conditions, Acta Mater. 75 (2014) 20-50.
[31] X. Lu, D. Wang, D. Wan, Z.B. Zhang, N. Kheradmand, A. Barnoush, Effect of electrochemical charging on the hydrogen embrittlement susceptibility of Alloy 718, Acta Mater. 179 (2019) 36-48.
[32] D. Wang, X. Lu, Y. Deng, D. Wan, Z. Li, A. Barnoush, Effect of hydrogen-induced surface steps on the nanomechanical behavior of a CoCrFeMnNi high-entropy alloy revealed by in-situ electrochemical nanoindentation, Intermetallics 114 (2019) 106605.
[33] D. Wang, X. Lu, D. Wan, Z. Li, A. Barnoush, In-situ observation of martensitic transformation in an interstitial metastable high-entropy alloy during cathodic hydrogen charging, Scr. Mater. 173 (2019) 56-60.
[34] S. Allain, P. Cugy, C. Scott, J.P. Chateau, A. Rusinek, A. Deschamps, The influence of plastic instabilities on the mechanical properties of a high-manganese austenitic FeMnC steel, Int. J. Mater. Res. 99(7) (2008) 734-738.
[35] J.E. Jin, Y.K. Lee, Strain hardening behavior of a Fe-18Mn-0.6C-1.5Al TWIP steel, Mater. Sci. Eng. A 527(1-2) (2009) 157-161.
[36] T. Depover, T. Hajilou, D. Wan, D. Wang, A. Barnoush, K. Verbeken, Assessment of the potential of hydrogen plasma charging as compared to conventional electrochemical hydrogen charging on dual phase steel, Mater. Sci. Eng. A 754 (2019) 613-621.
[37] C. Verpoort, D.J. Duquette, N.S. Stoloff, A. Neu, The Influence of Plastic-Deformation on the Hydrogen Embrittlement of Nickel, Mater. Sci. Eng. 64(1) (1984) 135-145.
[38] D.P. Abraham, C.J. Altstetter, The Effect of Hydrogen on the Yield and Flow Stress of an Austenitic Stainless Steel, Metall. Mater. Trans. A 26(11) (1995) 2849-2858.
[39] D.F. Teter, I.M. Robertson, H.K. Birnbaum, The effects of hydrogen on the deformation and fracture of beta-titanium, Acta Mater. 49(20) (2001) 4313-4323.
[40] G.M. Bond, I.M. Robertson, H.K. Birnbaum, Effects of Hydrogen on Deformation and Fracture Processes in High-Purity Aluminum, Acta Metall. 36(8) (1988) 2193-2197.
[41] A.C. Mackenzie, J.W. Hancock, D.K. Brown, On the influence of state of stress on ductile failure initiation in high strength steels, 9(1) (1977) 167-188.

[42] D. Wan, A. Alvaro, V. Olden, A. Barnoush, Hydrogen-enhanced fatigue crack growth behaviors in a ferritic Fe-3wt%Si steel studied by fractography and dislocation structure analysis, Int. J. Hydrog. Energy 44(10) (2019) 5030-5042.
[43] X. Lu, D. Wang, Effect of hydrogen on deformation behavior of Alloy 725 revealed by in-situ bi-crystalline micropillar compression test, Journal of Materials Science & Technology (2020).
[44] M. Koyama, E. Akiyama, K. Tsuzaki, Effect of hydrogen content on the embrittlement in a Fe–Mn–C twinning-induced plasticity steel, Corros. Sci. 59 (2012) 277-281.
[45] A.E. Pontini, J.D. Hermida, X-ray diffraction measurement of the stacking fault energy reduction induced by hydrogen in an AISI 304 steel, Scr. Mater. 37(11) (1997) 1831-1837.
[46] I.J. Park, K.H. Jeong, J.G. Jung, C.S. Lee, Y.K. Lee, The mechanism of enhanced resistance to the hydrogen delayed fracture in Al-added Fe-18Mn-0.6C twinning-induced plasticity steels, Int. J. Hydrog. Energy 37(12) (2012) 9925-9932.
[47] V. Olden, C. Thaulow, R. Johnsen, Modelling of hydrogen diffusion and hydrogen induced cracking in supermartensitic and duplex stainless steels, Mater. Des. 29(10) (2008) 1934-1948.
[48] J.A. Ronevich, S.K. Kim, J.G. Speer, D.K. Matlock, Hydrogen effects on cathodically charged twinning-induced plasticity steel, Scr. Mater. 66(12) (2012) 956-959.
[49] K.E. Nygren, K.M. Bertsch, S. Wang, H. Bei, A. Nagao, I.M. Robertson, Hydrogen embrittlement in compositionally complex FeNiCoCrMn FCC solid solution alloy, Curr. Opin. Solid State Mater. Sci. 22(1) (2018) 1-7.
[50] M. Seita, J.P. Hanson, S. Gradečak, M.J. Demkowicz, The dual role of coherent twin boundaries in hydrogen embrittlement, Nat. Commun. 6(1) (2015) 6164.
[51] X. Lu, Y. Ma, D. Wang, On the hydrogen embrittlement behavior of nickel-based alloys: Alloys 718 and 725, Mater. Sci. Eng. A 792 (2020) 139785.
[52] S. Bechtle, M. Kumar, B.P. Somerday, M.E. Launey, R.O. Ritchie, Grain-boundary engineering markedly reduces susceptibility to intergranular hydrogen embrittlement in metallic materials, Acta Mater. 57(14) (2009) 4148-4157.
[53] A. Oudriss, J. Creus, J. Bouhattate, E. Conforto, C. Berziou, C. Savall, X. Feaugas, Grain size and grain-boundary effects on diffusion and trapping of hydrogen in pure nickel, Acta Mater. 60(19) (2012) 6814-6828.
[54] T. Watanabe, The impact of grain boundary character distribution on fracture in polycrystals, Mater. Sci. Eng. A 176(1) (1994) 39-49.
[55] I. Gutierrez-Urrutia, S. Zaefferer, D. Raabe, Electron channeling contrast imaging of twins and dislocations in twinning-induced plasticity steels under controlled diffraction conditions in a scanning electron microscope, Scr. Mater. 61(7) (2009) 737-740.
[56] B.A. Wilcox, G.C. Smith, Intercrystalline fracture in hydrogen-charged nickel, Acta Metall. 13(3) (1965) 331-343.
[57] H. Abdolvand, A.J. Wilkinson, Assessment of residual stress fields at deformation twin tips and the surrounding environments, Acta Mater. 105 (2016) 219-231.
[58] Y. Zhang, P.C. Millett, M. Tonks, B. Biner, Deformation-twin-induced grain boundary failure, Scr. Mater. 66(2) (2012) 117-120.
[59] D. Wan, A. Barnoush, Plasticity in cryogenic brittle fracture of ferritic steels: Dislocation versus twinning, Mater. Sci. Eng. A 744 (2019) 335-339.
[60] A. Oudriss, S. Le Guernic, Z. Wang, B. Osman Hoch, J. Bouhattate, E. Conforto, Z. Zhu, D.S. Li, X. Feaugas, Meso-scale anisotropic hydrogen segregation near grain-boundaries in polycrystalline nickel characterized by EBSD/SIMS, Mater. Lett. 165 (2016) 217-222.
[61] A. Metsue, A. Oudriss, X. Feaugas, Hydrogen solubility and vacancy concentration in nickel single crystals at thermal equilibrium: New insights from statistical mechanics and ab initio calculations, J. Alloys Compd. 656 (2016) 555-567.
[62] R.A. Oriani, P.H. Josephic, Equilibrium Aspects of Hydrogen-Induced Cracking of Steels, Acta Metall. 22(9) (1974) 1065-1074.

## Highlights

Tensile deformation of H-charged TWIP steel was investigated via *in-situ* SEM imaging

H-induced surface cracks were systematically investigated via SEM techniques

An innovative approach was proposed for determining the true stress level

H was found to have a hardening effect on the TWIP steel

The threshold H concentration for ductile-to-brittle transition was determined by TDS

**Declaration of interests**

☒ The authors declare that they have no known competing financial interests or personal relationships that could have appeared to influence the work reported in this paper.

☐The authors declare the following financial interests/personal relationships which may be considered as potential competing interests: